Remote Sensing of Environment 264 (2021) 112614

Contents lists available at ScienceDirect

Remote Sensing of Environment

journal homepage: www.elsevier.com/locate/rse

Assessment of ocean wave spectrum using global Envisat/ASAR data and hindcast simulation

Huimin Li [a,*], Justin E. Stopa [b], Alexis Mouche [c], Biao Zhang [a], Yijun He [a], Bertrand Chapron [c]

[a] School of Marine Sciences, Nanjing University of Information Science and Technology, Nanjing, China
[b] Department of Ocean and Resources Engineering, University of Hawaii at Manoa, Honolulu, HI, USA
[c] Ifremer, Univ. Brest, CNRS, IRD, Laboratoire d'Océanographie Physique et Spatiale (LOPS), IUEM, Brest, France

ARTICLE INFO

Editor: Dr. Menghua Wang

Keywords:
Envisat/ASAR wave mode observations
SAR image spectral parameter
Spectral assessment

ABSTRACT

Wave mode of spaceborne synthetic aperture radar (SAR) is designed for the global ocean wave observations. Despite the fact that the significant wave height inferred from SAR measurements has been validated against model output and *in-situ* data, SAR's primary and unique capability for operational 2-dimensional spectral description of sea state remains to be fully evaluated. In this study, we extended the previous assessment approaches by introducing a new SAR image spectral parameter, the Mean rAnge Cross-Spectrum (MACS) that focuses on the isolated wave scales along the radar line-of-sight direction. MACS is an efficient variable in that it characterizes the local wave spectra properties without need of the non-linear wave inversion procedure. The assessment is based on the multiple-year data acquired by Envisat/ASAR wave mode, along with the collocated WaveWatch III (WW3) hindcast and the *in-situ* buoy-observed wave spectra, for which the SAR forward transformation is systematically performed to obtain the simulated image spectra. Inter-comparison between SAR-measured and WW3-simulated MACS demonstrates that the consistency is wavelength (or wavenumber) dependent. Three typical wavelengths, around 62 m for windsea, 168 m for intermediate waves and 342 m for swell, are selected to present the MACS comparison in detail. Comparable magnitude of SAR-measured and the simulated MACS is observed for the intermediate waves and swell, while larger simulation values are predicted for the windsea waves. Spatial distribution of MACS agrees well between these two data sets for all wavelengths with high correlation coefficients (>0.8) in most of the global ocean. One exception is in the extratropics where the quantitative difference is particularly notable. In the contrary, when comparing SAR-measured and buoys-simulated MACS, the agreement increases towards the shorter (<100 m) wavelengths. We also found that the large-scale atmospheric/oceanic features persistent on SAR images lead to the overestimate of SAR MACS at long wavelengths, which is expected to bias the wave inversion. The wave spectra retrieval performance shall advance as long as such impact is properly resolved.

1. Introduction

Sea state information is crucial to managing the ocean resources and safe operations for the ocean going activities. Global wave information has been paramount in understanding the wind and wave patterns including their regional variability (Young, 1999). Among the various means of observations, satellite altimeters measuring the global significant wave heights reaches an accuracy of 30 cm relative to the *in-situ* buoy observations (Queffeulou, 2004; Zieger et al., 2009; Quach et al., 2020). These data have greatly helped the development, calibration, and validation of numerical spectral wave models with improved predictability (Ardhuin et al., 2010; Stopa et al., 2016b). While this information is important to monitor the regional change (Young et al., 2011), they are not sufficient to fully represent the sea state conditions, particularly for multimodal wave systems. Active radars, such as real aperture radars (RAR) and synthetic aperture radars (SAR) are the operational spaceborne sensors to measure both the wavelength and wave directions at global scales. Of which, SAR is advantageous in, on one hand, that its high spatial resolution allows to resolve the short wind waves. On the other hand, the operation of SAR sensors since 1990s provides the temporal data series for extensive wind-wave study at global scale.

* Corresponding author.
E-mail address: huimin.li@nuist.edu.cn (H. Li).

https://doi.org/10.1016/j.rse.2021.112614
Received 30 November 2020; Received in revised form 14 July 2021; Accepted 16 July 2021
Available online 30 July 2021

A SAR emits microwave pulses and precisely measure their Doppler-shifted returns. Since the ocean surface is in continuous motion, the radar returns are often misplaced when converted from the Doppler-frequency domain to the geo-referenced images in space domain. This misplacement leads to the nonlinear distortions of wave signatures in the along-track direction, referred to as the azimuth cutoff (Kerbaol et al., 1998). When the local wind forcing is calm to moderate, the azimuth cutoff wavelength is usually shorter than the swell components, enabling to uniquely estimate both the wavelength, direction and spectral energy of swell systems with SAR observations (Collard et al., 2009; Ardhuin et al., 2017). Note that the high frequency waves in the along-track directions are often distorted. This has motivated several studies to directly estimate the significant wave height (SWH) from SAR images using empirical methods, which is particularly successful for Sentinel-1 acquisitions with high accuracy (Schulz-Stellenfleth et al., 2007; Stopa and Mouche, 2017; Rikka et al., 2018; Pleskachevsky et al., 2019; Quach et al., 2020). However, the direction and wavelength information is lost especially for waves traveling along the flight at wavelengths shorter than the azimuth cutoff which is typically 150–200 m for C-band SAR with an altitude of 700 km. (Li and Saulter, 2012) compared the subrange SWH integrated over the distinct wave scales, rather than the overall SWH of advanced-SAR (ASAR) aboard Envisat satellite relative to buoys and models. Their approach in (Li and Saulter, 2012) validates SAR observations in terms of the subrange wave height, but relies on the operational quasi-linear inversion scheme (Krogstad et al., 1994). It is worth noting that such a scheme is not able to fully recover the nonlinear distortions (Krogstad et al., 1994). So far, the validations of SAR observations regarding the ocean wave spectrum (short for the ocean wave height spectrum) retrieval are based on either total or effective SWH. The inversed wave spectra has not yet been assessed in terms of their spectral features relative to the reference data.

In the cross-track direction (range) of SAR image coordinate, the distortion is less strong and the mapping could be approximated as a quasi-linear process. The Mean rAnge Cross-Spectra (MACS) introduced by (Li et al., 2019a, 2019b) has shown its reliability in describing up to 20 m range-traveling waves Sentinel-1 (S-1) C-band SAR. This parameter represents the SAR image cross-spectrum values averaged over the azimuthal wavenumbers in the range of $[-2\pi/600rad\cdot m^{-1}, 2\pi/600rad\cdot m^{-1}]$ and offers opportunities to investigate the wave information of isolated wave scale in the range direction. By definition, MACS focuses on the SAR image cross-spectrum where the quasi-linear mapping applies. Therefore, one advantage of using MACS is there is no need to go through the non-linear SAR inversion scheme or perform the hypothesis of a quasi-linear imaging mechanism. As a complementary study to the SWH assessment (Li and Saulter, 2012), we attempt to evaluate the wave spectral signatures through MACS of ASAR observations with respect to the wave spectral model output and *in-situ* buoy measurements. Using this approach can potentially lead to a better understanding of the wave dynamics while assessing the SAR and spectral wave model, WW3 (The WAVEWATCH III® Development Group). In order to carry out the comparison of MACS between SAR and WW3/buoy, we implement the nonlinear forward SAR mapping transformation in (Engen and Johnsen, 1995) for given ocean wave spectra and SAR configurations to obtain the simulated SAR image spectra. In this study, following the general assessment strategy of integral wave height (Young, 1999; Li and Saulter, 2012), the quantitative relationship of MACS parameter for various wavelengths is examined between WW3-simulation and SAR measurements. The global signatures of SAR MACS relative to the simulation is also investigated and discussed to highlight their spatial consistency. An independent comparison with buoy observations is invoked to further interpret the inter-comparison results between ASAR and the collocated WW3-simulation.

Specifically in this study we use the two-dimensional wave spectra simulated from a hindcast (Stopa et al., 2019) and measured by buoys to derive the equivalent MACS values to be compared with Envisat/ASAR observations from 2002 to 2012. We take benefit of this entire decade of SAR data to statistically compare MACS obtained at various wavelengths and at global scale. The manuscript is organized as follows. In Section 2 we describe the data sets and methodology: forward SAR transformation and MACS definition. In Section 3, we present the MACS comparison between ASAR measurements and the simulation from the WW3 hindcast and buoy ocean wave spectra. Discussions and conclusions follow in Sections 4 and 5, respectively.

2. Data and MACS definition

In this section, we first describe the Envisat/ASAR data and wave spectra from the numerical wave model. Next we describe the forward SAR transformation used to map the wave spectra into an equivalent image cross-spectra. Lastly we describe the estimation of MACS from a SAR image cross-spectra.

2.1. Envisat/ASAR wave mode

Envisat/ASAR operated for nearly a decade from November 2002 to April 2012. It is a C-band radar (center frequency of 5.33 GHz), collecting SAR images in various modes. Wave mode is dedicated to observing the global ocean waves (Hasselmann et al., 2012). The wave mode vignettes are acquired every 100 km along the track, having the spatial footprint of 10 km × 7 km (azimuth by range) with the pixel spacing of 9 m × 6 m. In this work, we use the wave mode images acquired at incidence angle of 23° and in VV polarization.

The SAR image cross-spectrum are systematically processed from the single look complex (SLC) SAR images, which are stored in the Level-1B products. In this study, the cross-spectral data set distributed by the European Space Agency (ESA) are utilized. Each image spectrum is composed of 24 discrete wavenumbers ranging from 0.008 rad·m^{-1} to 0.2 rad·m^{-1} and 36 direction in the range of [0°, 360°] (Johnsen, 2005). The images acquired between the January 2007 and April 2012 are collocated with the operational ECMWF (European Centre for Medium-Range Weather Forecasts) analysis wind vectors (Nagarajan and Aiyyer, 2004). The reanalysis product is available at a spatial resolution of 0.5° every 6 h (0 h,6 h,12 h,18 h at UTC time). The wind vector at the nearest spatial and temporal point to the SAR passing time is taken as the reference wind of each SAR image.

2.2. Hindcast ocean wave spectra

The wave spectra are generated from version 5.16 of the spectral wave model WW3 (The WAVEWATCH III® Development Group). We use the parameterizations of wave generation and dissipation proposed by (Ardhuin et al., 2010) and the non-linear Discrete Interaction Approximation by (Hasselmann and Hasselmann, 1985). It has been shown that this model configuration works well for H_s and swell partitions in comparison to other parameterization packages (Stopa et al., 2016a). The global model is implemented at the latitude and longitude grid of 0.5° with a spectral bin composed of 24 directions and 32 frequencies that are exponentially spaced from 0.037 Hz to 0.7 Hz at an increment of 10%. The wind and ice fields at a spatial resolution of 0.2° (22 km) from the Climate Forecast System Reanalysis (CFSR) (Saha et al., 2010, 2014) are used to force the model runs. The hindcast was calibrated and corrected in time to match a homogenized satellite altimetry database of (Queffeulou and Croizen-Fillon) (Stopa, 2018; Stopa et al., 2019).

We output the wave spectra directly for each longitude, latitude, and time corresponding to the Envisat/ASAR acquisition. The minimum wavelength of WW3 wave spectra is 3.2 m (0.7 Hz), smaller than the wave mode resolution (9 m). This would ensure that all wavelengths resolved by SAR are comparable with those of the WW3 wave spectra.

2.3. Buoy observations

The wave measurements from the National Data Buoy Center (NDBC) are used in this study as complementary to the SAR observations and model outputs. A triple collocation data set is created by limiting the spatial distance between the center of SAR images and the location of buoys within 100 km and the temporal window shorter than 30 mins. It ends up with 1218 valid collocation pairs.

The wave spectra measured by NDBC buoys, is composed of frequencies from 0.04 Hz up to 0.4850 Hz (Vandemark et al., 2005). We employed the Maximum Entropy Method (MEM) proposed in (Lygre and Krogstad, 1986) to reconstruct the two-dimensional wave spectra from estimates of the Fourier coefficients. In specifics, this includes $\alpha 1$ that represents the mean wave direction, $\alpha 2$ that denotes the dominant wave direction, and $r1$ and $r2$ that describe the directional spreading relative to the main direction. For simplicity, the directional bin for buoy wave directional spectral reconstruction is set to be 10° throughout rest of this paper unless otherwise stated.

2.4. SAR forward transformation

The SAR forward transformation maps a wave spectrum into a SAR image cross-spectra, which is calculated using the two sub-looks during the SAR integration time. The imaginary component is associated to the wave motion within the time difference between the two sub-looks. It is therefore widely used to remove the 180° direction ambiguity of the swell propagation (Engen and Johnsen, 1995). In addition, the cross spectra helps filter non-coherent signals typically improving the signal-to-noise ratio of ocean waves.

(Engen and Johnsen, 1995) presented the derivation of SAR image cross-spectra in detail using the general formula for the nonlinear mapping:

$$P_S^{mn}\left(\vec{k},\Delta t\right) = \int d\vec{x}\; e^{-i\vec{k}\cdot\vec{x}}\; e^{k_x^2\left[\rho_{aa}\left(\vec{x},t\right)-\rho_{dd}\left(\vec{0},0\right)\right]}\left[1+\rho_{II}\left(\vec{x},t\right)\right] \tag{1}$$

where the subscript a and I in ρ_{aa} denote the velocity bunching and the real aperture radar (RAR) modulation, respectively. k_x is the wavenumber along the azimuth direction. The correlation function defined in Eq. (1) is related to the ocean wave spectrum $S\left(\vec{k}\right)$ through

$$\rho_{aa}(\vec{x},\Delta t) = \frac{1}{(2\pi)^2}\int d\vec{k}\; e^{i\vec{k}\cdot\vec{x}}\cdot\frac{1}{2}\left[\left|M_a\left(\vec{k}\right)\right|^2 e^{-i\omega\Delta t}S\left(\vec{k}\right) + \left|M_a\left(-\vec{k}\right)\right|^2 e^{i\omega\Delta t}S\left(-\vec{k}\right)\right] \tag{2}$$

where M_a represents the modulation transfer function (MTF) for RAR or velocity bunching. The detailed formulation of MTF can be found in (Engen and Johnsen, 1995; Li et al., 2019a, 2019b). In this study, we define the MACS in terms of the real component of SAR image cross-spectra.

Four SAR roughness images acquired by Envisat/ASAR wave mode are shown in Fig. 1 (a1)-(a4). Real component of the measured SAR and simulated WW3 cross-spectra are accordingly given in (b1)-(b4) and (c1)-(c4). In general, the most energetic wave systems appear to agree

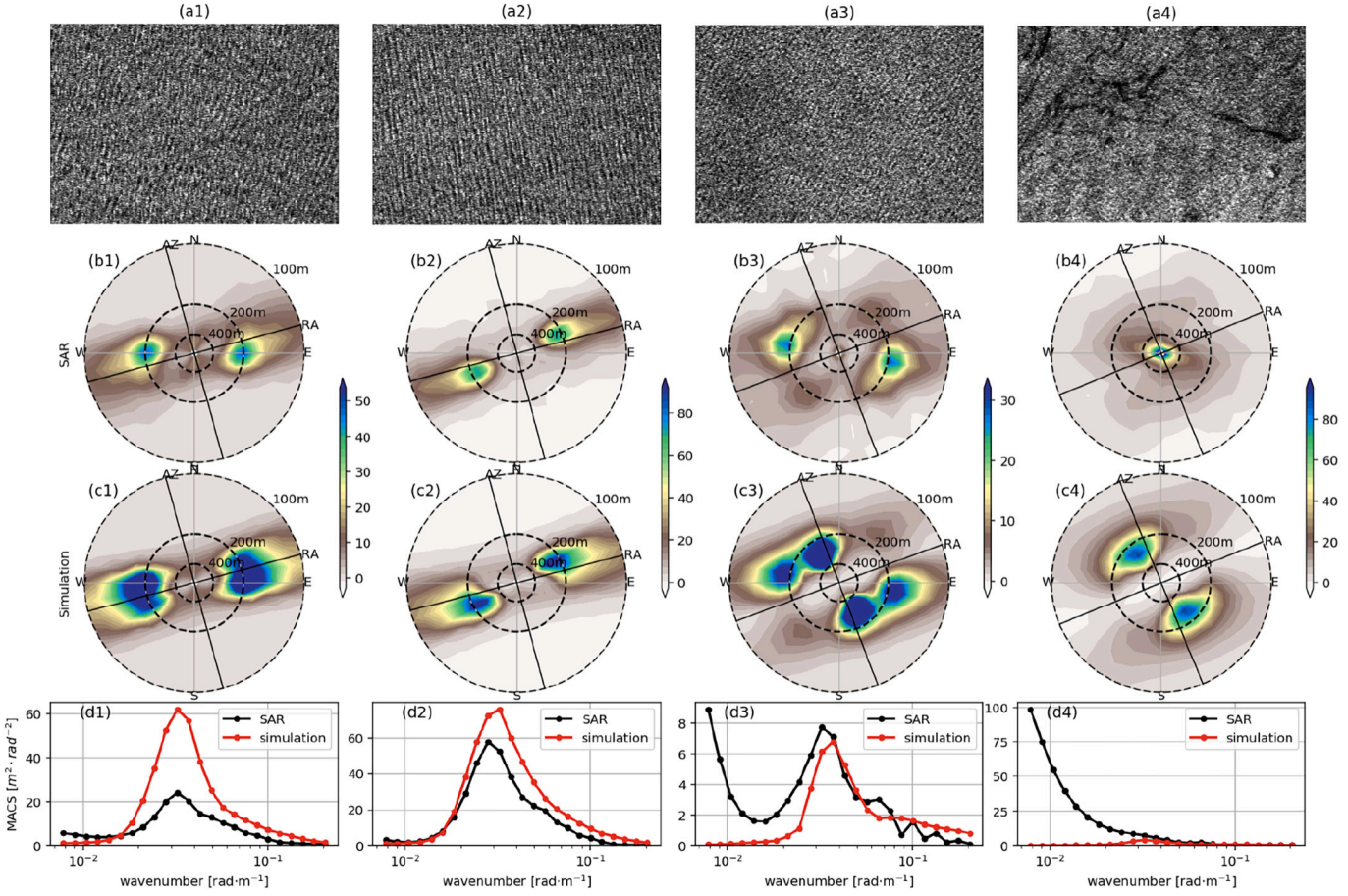

Fig. 1. Examples of ENVISAT/ASAR wave mode images for the definition of range MACS profile. The row (a1)-(a4) shows the SAR backscattering image. Real component of the SAR cross-spectra is given in the second row (b1)-(b4) and the corresponding simulated cross-spectra basedon the WW3 wave spectra and the forward SAR transformation is in the third row (c1)-(c4). The bottom row (d1)-(d4) shows the MACS profile representing the energy for wavenumbers along the SAR range direction.

well between the SAR and WW3 cross-spectra. Despite the matched spectral pattern, WW3 has overall larger values for the dominant waves. Note that in panel (b3)&(c3) of Fig. 1, a wave system along the SAR azimuh direction is predict by WW3, but not well resolved by the corresponding SAR observations. Also, though it is likely that the non-ocean waves patterns inducing large-scale modulation as observed in panel (a4) impacts the cross-spectral analysis, its quantitative influence still needs to be further investigated.

2.5. MACS profile extraction

In this manuscript, we follow the procedure of (Li et al., 2019a, 2019b) to define the MACS from both observations and simulations by

$$MACS(k) = \frac{1}{N}\int_A P_s(k,\phi), \quad A \in [\phi_{ra} - 10^\circ < \phi < \phi_{ra} + 10^\circ] \tag{3}$$

where $P_s(k,\phi)$ represents the cross-spectrum in polar coordinate. ϕ_{ra} is the SAR range direction. In this study, we extend our range of wave scales from 47 m to 800 m. The smallest wavelength is 47 m because the ASAR range spatial resolution is about 9 m and we use a factor of ≈5 to ensure the waves are properly resolved by the Fast Fourier Transform. The range profile (±15° relative to the line-of-sight) of SAR image cross-spectra for all wavenumbers is then extracted, denoted as MACS profile hereinafter. Fig. 1 bottom row shows the MACS profiles for these four representative cases. The overall MACS wavenumber distributions generally match, but there are noticeable differences in magnitude. In panel (d1) and (d2) of Fig. 1, the simulated MACS profiles have larger values than that of the observations. In panel (d3), the SAR exhibits higher MACS energy for wavelengths longer than 400 m. While in panel (d4), SAR MACS is constantly larger for the wavelengths longer than 150 m. This is clearly due to the presence of the large-scale phenomenon as observed in the SAR image in the subplot of (a4). MACS can be computed for any wavelength bins between 30 m and 800 m with ASAR. Hereinafter, we denote as $MACS_\lambda$ for each isolated wavenumber/wavelength component where λ is the wavelength. For example $MACS_{62}$, represents MACS for the wavelength of 62 m.

Envisat is a polar orbit satellite, with both ascending (flying from South Pole to the North Pole) and descending trajectories. Since MACS only focuses on the wave signatures along the radar range axis, in other words, the spatial pattern of MACS between the two passes represents waves in different direction. Given that the global MACS is expected to highlight the local winds conditions strongly coupled to the waves signatures of interest, combination of both ascending and descending observations shall complicate the spatial analyses. We first demonstrate the comparison of $MACS_{62}$ in Fig. 2 and it turns out their spatial patterns presents strong similarity. Yet differences does exist. The most noteworthy occurs off the west coast of Arabian Sea where the Indian monsoon reverses the wind direction from summer to winter. Given the radar configuration, the radar line-of-sight of the ascending pass is roughly in alignment with the wind blowing direction, while the descending pass sees a direction deviation about 30°. This looking direction results in the smaller $MACS_{62}$ for the descending pass as shown in Fig. 2(c). In addition, the ascending pass seems to capture $MACS_{62}$ at broader extent over the trade winds region in the Pacific Ocean. The $MACS_{62}$ of descending pass has higher values in the Southern Ocean also because of the favorable wind direction. As for the average MACS profile in Fig. 2(b) and (d), the median values between these two passes are comparable. Given the strong similarity of MACS profile between the ascending and descending pass, only the observations from the ascending pass are included in the following assessment relative to the model hindcast output with a total number of SAR images around 3×10^6.

3. Results

In this section, we examine the consistency of MACS profile between the SAR-observations and WW3-simulations. Taking advantage of the versatility of MACS, we analyze the statistical relationship as well as the global patterns of MACS at three typical wavelengths of 62 m for short

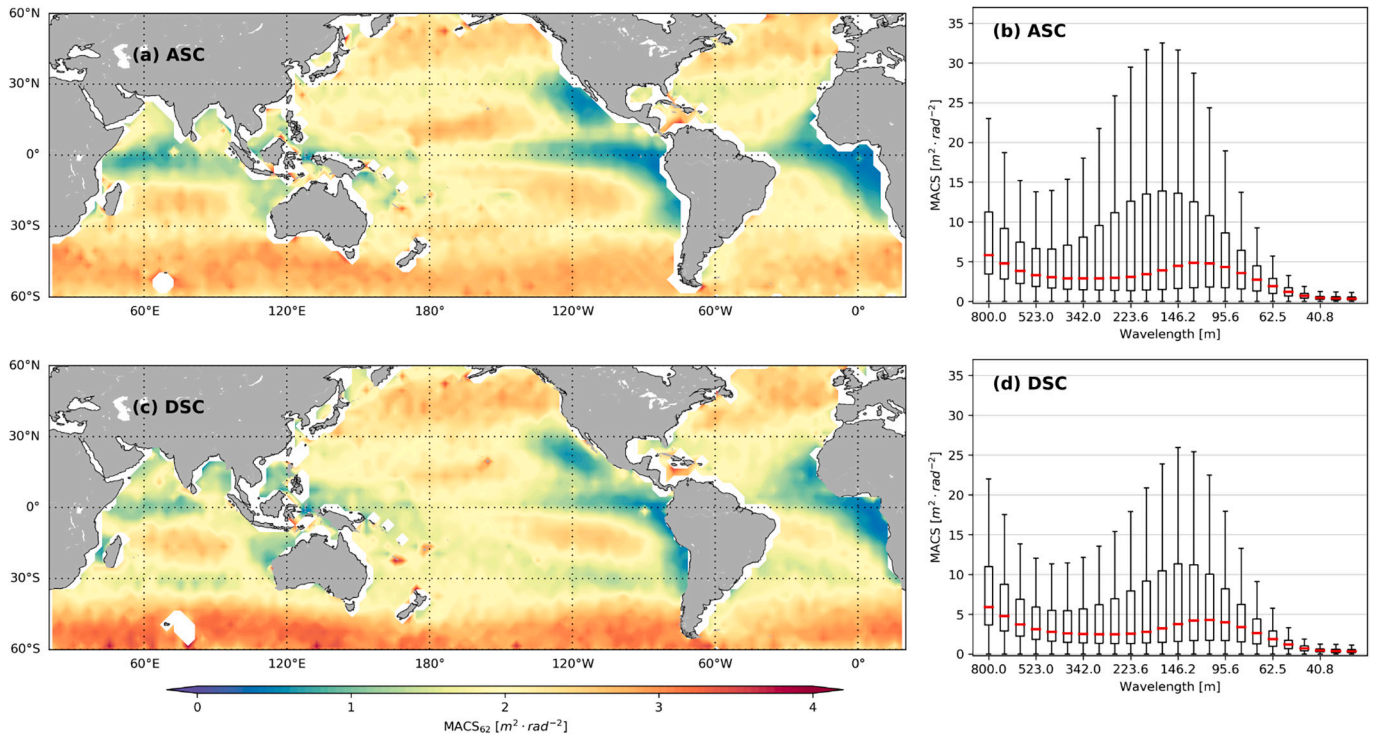

Fig. 2. Comparison of global $MACS_{62}$ for (a) ascending pass and (c) descending pass. The averaged MACS profile relative to the wavenumber is given in (b) ascending pass and (d) descending pass. Note that this figure is created based on the observations in the years of 2010 and 2011. The latitude and longitude bin of 3° is set to compile the global map.

wind sea, 168 m for intermediate ocean waves and 342 m for long swell. We also carried out the MACS comparisons with buoy wave measurements as an attempt of interpreting the differences found between the SAR and WW3-simulation.

3.1. MACS profile

MACS profiles of the SAR-observation and WW3-simulations between January 2007 and April 2012 are presented in the box plot relative to wavelengths in Fig. 3. For each wavelength, the box shows the distribution of that particular $MACS_\lambda$. The central box represents the likely range of variation: the interquartile range, *IQR*. The whisker extends to the largest and smallest data value within $1.5 \times IQR$ from the lower and upper quartile, respectively. SAR-measured MACS profile shares a couple of commonality with that of the WW3-simulation. First, for most of the wavelengths, MACS is not normally distributed as the distance of the median to the upper quartile is much larger than that to the lower quartile. In other words, MACS is generally right-skewed with smaller median (red segment) than the mean (blue curve). The mean and median are largely apart except over the shorter wavelengths (<62 m) where these two are almost identical. Peaks of the profile also differ as the mean locates at 223 m and the median at 95 m. The maximum *IQR* locates at the wavelength of 168 m, distinct from both the median and the mean. Despite the resembling distributions of MACS for each wave scales between SAR and WW3, they differ in several aspects. SAR-measured MACS profile in Fig. 3(a) has a clear increase towards longer wavelengths beyond 523 m for mean, median and *IQR*. While the WW3-simulation shows a consistent MACS decrease towards both longer and shorter wavelengths from the peak. Both data sets have comparable mean MACS values except for the very long wavelengths. It is not the case for the median and *IQR*. For wavelengths shorter than 250 m, the WW3-simulated *IQR* is larger than the SAR measurement. As for the median, the WW3 exceeds at the wavelengths shorter than 146 m. The distribution of WW3-simulated MACS at one particular wavelength roughly follows a negative exponential function, while the SAR-measured is a log-normal curve (not shown). In any case, the smaller *IQR* suggests a less spread distribution. On the other hand, for wavelengths longer than 250 m, the slow variation of SAR MACS might result from the impact of large-scale oceanic and atmospheric phenomena as displayed in Fig. 1(a4)-(d4). This also possibly results in the large spread of SAR-measured MACS than its counterpart based on the WW3-simulation.

Going further, we now focus on the observed and simulated MACS for short (62 m), intermediate (168 m) and long (342 m) waves. As displayed in Fig. 3, MACS at the wavelength of 168 m has both comparable mean and median between SAR and WW3. MACS of 62 m exhibits smaller values in SAR observations than WW3 simulations, while it is the opposite trend for MACS at 342 m. The Q-Q plots of SAR-measured MACS relative to the simulation for these three selected wavelengths are presented in Fig. 4. For 62 m as shown in Fig. 4(a), WW3-simulation is consistently higher than that of SAR with most of the data points well above the one-to-one line. If we neglect the saturation of SAR MACS beyond 4 $m^2 \cdot rad^{-2}$, slope of the linear fit to these points approximates the value of 2. It means that for most of the SAR acquisitions, the predicted MACS by WW3 is twice larger than the SAR observations. As for the wavelength of 168 m shown in Fig. 4(b), the agreement improves as most of the data points scatter around the one-to-one line. It should be noted that the mean curve (dashed line) slightly deviates from a linear variation. While for the wavelength of 342 m in Fig. 4(c), the mean curve is indeed well following the one-to-one curve. However, the MACS relationship is largely dispersed as represented by the greater standard deviation. The standard deviation of $MACS_{342}$ in Fig. 4 gradually increases with the magnitude of $MACS_{342}$. For the other two wavelengths, the standard deviation is almost constant from small to large MACS values. In particular, very small MACS values are predicted by WW3-simulation as shown by the large number of data points clustered close to the horizontal axis in Fig. 4(c). With this statistical comparison in mind, we also examined the spatial consistency between MACS of these two data sets to further diagnose the regional variation of their agreements. The comparison of global MACS for these three selected wavelengths are therefore analyzed in the following.

3.2. Spatial analyses of MACS

We also compute global maps of the three representative $MACS_{62}$, $MACS_{168}$, and $MACS_{342}$ typical of the short, intermediate and long ocean waves, respectively. In the qualitative terms, the global patterns of SAR-observed and WW3-simulated MACS are similar. The global averaged MACS at wavelength of 62 m from SAR-observations (left) and WW3-simulations (right) is given in the top panel of Fig. 5. As shown, the spatial signatures mimic that of the overall wind field (Young, 1999) as these short waves are closely coupled with the moderate wind speeds around $8\ m \cdot s^{-1}$ (Hasselmann et al., 1973). Smaller values of $MACS_{62}$ are observed over the Inter Tropical Convergence Zone (ITCZ) where the wind speed is relatively low throughout the year (Žagar et al., 2011). Over the extratropics, larger $MACS_{62}$ is found generated by the high wind events associated to the frequent low-pressure storm activities. However, the SAR-observed MACS is systematically smaller than the

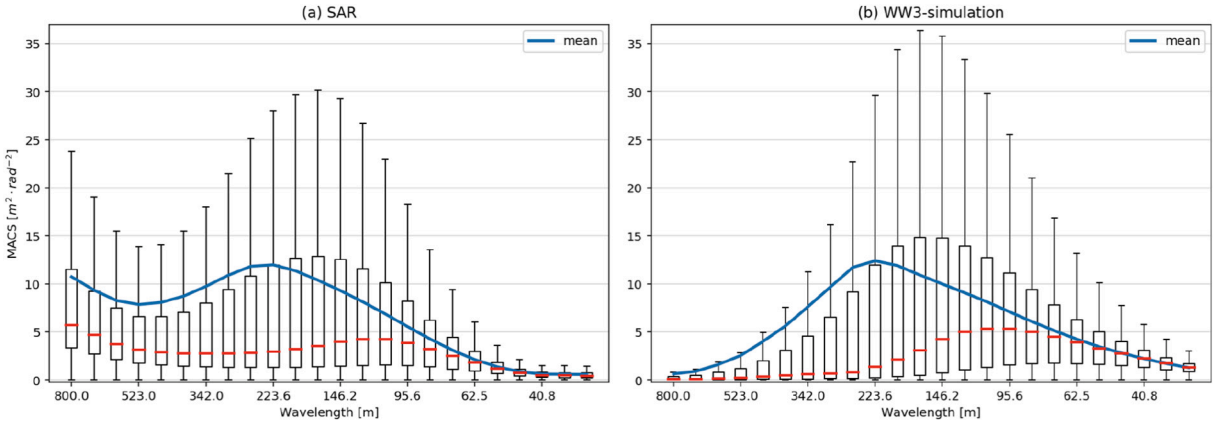

Fig. 3. Box plot of the MACS profile from (a) SAR-observation; (b) WW3-simulation with respect to the wavelengths. For MACS at given wavelength, each rectangle spans the first quartile to the third quartile (the interquartile range, *IQR*). The red segment inside rectangles denotes the median. The upper whisker extends to the largest data value within $1.5 \times IQR$ above the third quartile and the lower to the smallest value within $1.5 \times IQR$ below the first quartile. The blue curve represents the mean for each wavelength/wavenumber. (For interpretation of the references to color in this figure legend, the reader is referred to the web version of this article.)

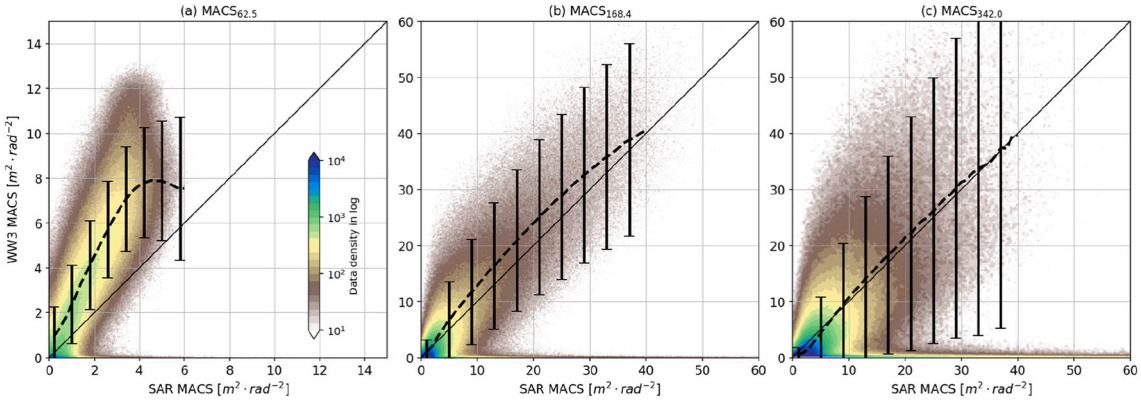

Fig. 4. Q-Q plot of MACS comparison between SAR-measured and WW3-simulated for the three typical wavelengths (a) 62 m; (b) 168 M; (c) 342 m. The dashed lines are the mean curve and the error bar stands for the one standard deviation. Color denotes the data count in log scale.

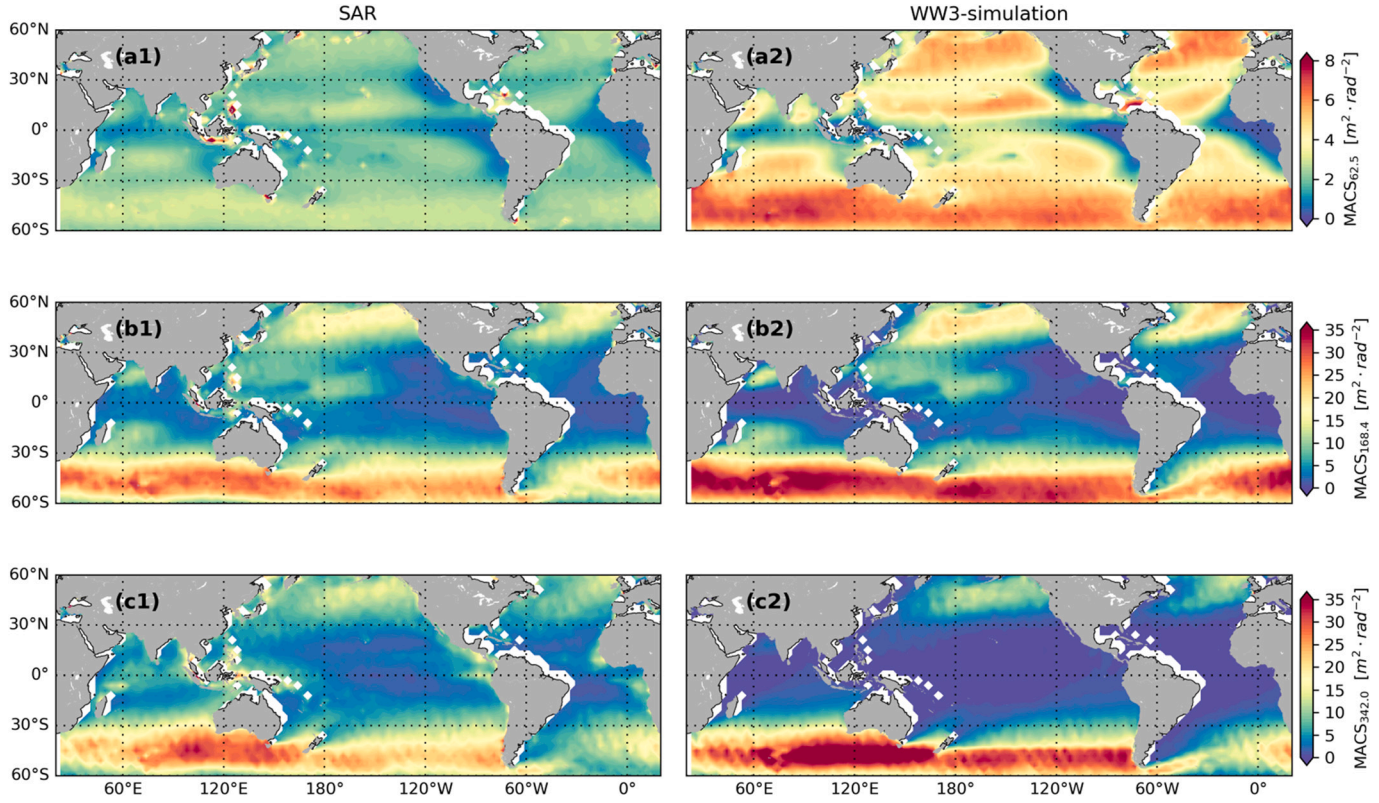

Fig. 5. Global average of MACS from (left) the SAR-measured and (right) the WW3-simulated for (top) 62 m; (middle) 168 m and (bottom) 342 m. Both latitude and longitude are binned into the grid of 2.5° by 2.5°. The bins located within 50 km from the coastline are masked as blank space. Color denotes the magnitude of MACS and note that the color bar dynamics differ among the three panels.

WW3-simulated values across the globe, consistent with Figs. 3 and 4(a). For example, in the Southern Ocean, WW3-simulated $MACS_{62}$ is around 6 $m^2 \cdot rad^{-2}$, which is twice as large as the SAR-observed $MACS_{62}$. Such trend of smaller SAR-observed MACS exists for all the wavelengths up to 150 m (not shown here for brevity). MACS of these two data sets becomes gradually closer as the wavelength increases to approximately 170 m (see Fig. 3).

$MACS_{168}$ is presented in the middle panel of Fig. 5. Overall, the WW3-simulated and SAR-observed $MACS_{168}$ are in good agreement in terms of the global pattern. $MACS_{168}$ is also consistently high (around 25 $m^2 \cdot rad^{-2}$) throughout the year in the southern extratropics. The trade wind regions exhibit reduced MACS magnitude in comparison to the extra-tropical regions. Yet, quantitative differences remain. Overestimates of the simulated MACS mainly locate in the extratropics, contrast to the global trend of $MACS_{62}$. Note that over the Arabian Sea, this overestimate is also evident during the monsoon season (seasonality not shown). It is thus speculated that WW3-simulation tends to predict larger spectral energy for 168 m waves at relatively high wind conditions. At low to median wind speed, the relative magnitude depends on the geographic locations. For example, SAR-observed $MACS_{168}$ generally exceeds the simulation in the East Equatorial Pacific Ocean. While in the Tropics, SAR-observed $MACS_{168}$ has larger values. This spatial pattern well corresponds to the feature presented in Fig. 4(b). Larger WW3-simulated $MACS_{168}$ is mostly observed for the larger MACS values, in other words at high sea state, like in the extratropics. While the larger SAR-observed $MACS_{168}$ mostly occurs at smaller MACS values as depicted by the blue cluster in Fig. 4(b).

At last, global average of $MACS_{342}$ is displayed in the bottom panel of

Fig. 5. It is expected that this longer wavelength relates to wind speeds approximately equivalent to 18 ms^{-1} (Hasselmann et al., 1973). Large $MACS_{342}$ values are mostly located in the extratropics, particularly in the Southern Hemisphere. Given the duration and fetch needed for the long waves to grow, $MACS_{342}$ are mostly observed in the east part of the Pacific and Atlantic Ocean, distinguished from the spatially distributed MACS for the the other two wavelengths. In the trade wind regions, the WW3-simulations show similar regional patterns as the SAR observations but with much lower magnitude. While in the extratropics, WW3-simulation exhibit larger MACS values throughout the year. This results in the scattered comparison and the large standard deviation in Fig. 4(c).

To further assess the difference in the geographical pattern, we computed the MACS magnitude ratio (SAR over WW3) as shown in Fig. 6. The ratio is uniformly smaller than 1 for $MACS_{62}$ across the globe shown in Fig. 6(a). This corresponds to the constantly larger WW3-simulation as presented in both Fig. 4 (left panel) and Fig. 5 (top panel). With the wavelength increasing, the MACS ratio shows significant spatial variability. For example, both $MACS_{168}$ and $MACS_{342}$ display lower values in the southern extratropics than the rest of the global surface in Fig. 6(b) and (c), respectively. In the contrary, the ratio of $MACS_{342}$ is very high (>6) in the trade winds regions due to the smaller WW3-simulation as observed in Fig. 5 bottom panel. It is worth noting that the straight boundary line at latitude of 45 ° S in Fig. 6(c) are present throughout the year. The sharp variation in Fig. 6 (b)(c) corresponds to the pattern shown in the WW3-simulation in Fig. 5(b2)(c2). While such variation is not found for the $MACS_{62}$ in Fig. 5(b1). Investigations of this abrupt alignment change shall be further addressed.

The Pearson correlation coefficients for MACS at 62 m, 168 m and 342 m are calculated from the monthly time series over each latitude/longitude bin of 2.5°, and shown in Fig. 7. As in Fig. 7(a), $MACS_{62}$ between the two data sets is highly correlated with correlation coefficient larger than 0.8 in most of the open ocean. Similarly, $MACS_{168}$ has strong correlation on the global scale, except over a narrow band at the equator (±10°) where the correlation coefficient decreases to 0.1 as in Fig. 7(b). The low correlation along the equator extends to the entire trade winds region, reaching ±30° for $MACS_{342}$ as in Fig. 7(c).

To further analyze the location-dependent correlations, three areas with each covering a 5° in both latitude and longitude are selected and annotated by the black rectangles in Fig. 7(c). The monthly time series of MACS for 62 m, 168 m and 342 m over each area are then plotted in top, middle and bottom panel of Fig. 8, respectively. The variation trend of temporal $MACS_{62}$ is found similar for both data sets except that the WW3-simulation shows consistently larger values. Despite that the simulated and observed MACS differentiate approximately by a factor of 2 over the time period, the co-variation results in the correlation coefficients higher than 0.70 for all these three areas. While for $MACS_{168}$ in the middle row, both data sets show comparable variation trends as well as quantitative values. Ocean waves of 168 m is better resolved than the 62 m in the calculation of SAR image cross-spectrum. This produces the high correlations (>0.80) found for all the three areas. Contrast to the shorter wavelength in Fig. 8(a1), MACS in (a2) exhibits much stronger seasonal changes. In winter, long ocean waves are generated by the high wind events associated with the winter storms and the averaged $MACS_{168}$ reaches up to 25 $m^{-2} \cdot rad^{-2}$. As the winter storms recede, the winds lowers and $MACS_{168}$ accordingly reaches the minimum values in summer close to zero. For the long waves of $MACS_{342}$, both R1 and R3 see consistent variation of SAR observation and WW3-simulation. Note that the WW3-simulation is greatly underestimated over R2 as shown in

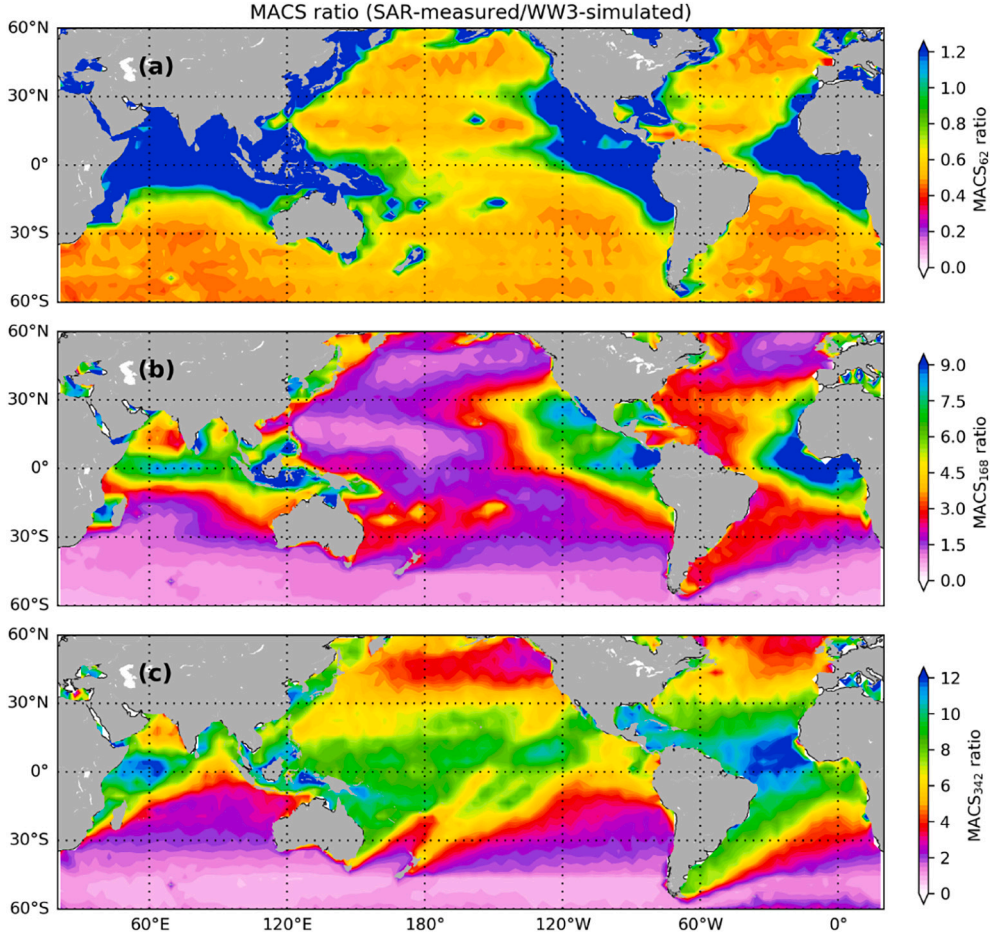

Fig. 6. Global ratio of MACS (SAR over WW3-simulation) for (a) 62 m; (b) 168 m; (c) 342 m. The latitude/longitude bin of 2.5° is used in this figure.

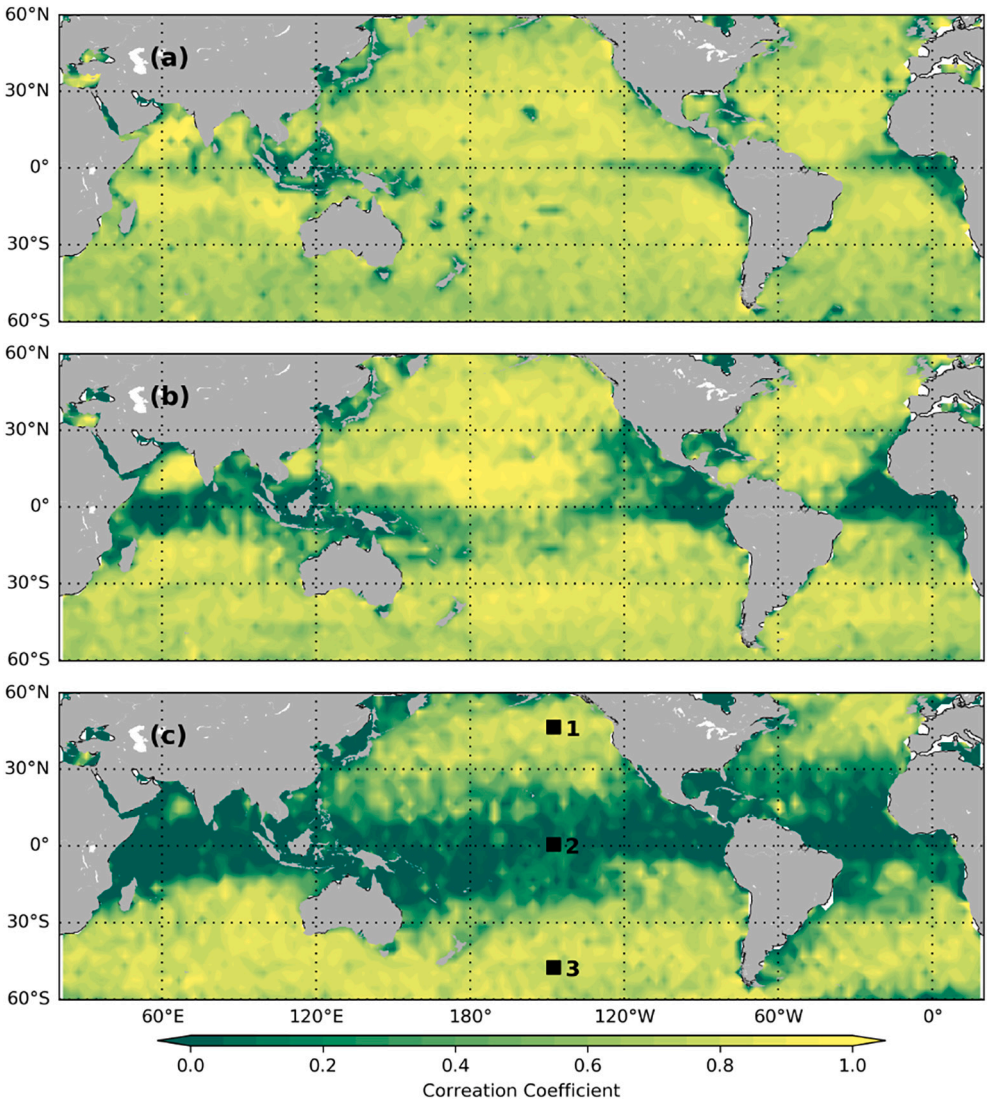

Fig. 7. Global correlation coefficients of MACS between SAR measurements and WW3-simulation for (a) 62 m; (b) 168 m; (c) 342 m. The latitude/longitude bin of 2.5° is used in this figure. The three black rectangle indicate the areas selected for further detailed correlation analysis.

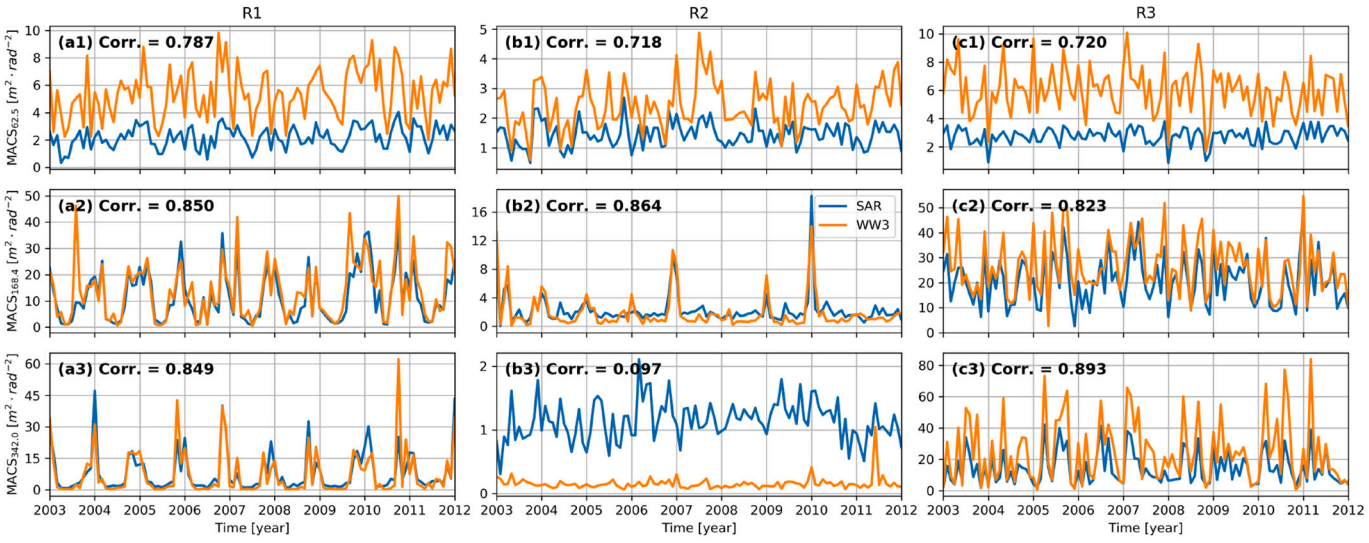

Fig. 8. Time series for MACS over the three selected areas annotated in Fig. 7, from left to right are R1, R2 and R3, respectively. For each area, from top to bottom are 62 m, 168 m and 342 m. The correlation coefficient is accordingly given in each plot.

Fig. 8(b3), resulting in the lower correlation coefficient of 0.097. This agrees well with the smaller MACS ratio in Fig. 6(c). We attributed this discrepancy to the pollution of SAR-observed MACS by the atmospheric or air-sea interaction features, including the rain impact and wind streaks et al. In fact, high occurrence of such phenomena has been detected by the automatic classification of Sentinel-1 SAR wave mode data (Wang et al., 2019) and particularly in the Tropics.

3.3. Triple comparison with buoy measurements

The global signatures of MACS strongly resemble between both data sets. Meanwhile it is found that the WW3-simulation is generally larger than the SAR-measured MACS. This quantitative difference also depends on the spatial locations at the globe. Taking advantage of the numerous Envisat/ASAR acquisitions, a triple comparison between SAR, WW3 and buoy measurements is carried out to further diagnose the difference between these data sets.

To extend the inter-comparison with the *in-situ* measurements, the NDBC wave buoys that are capable of obtaining the two-dimensional wave spectrum are collocated with the Envisat/ASAR wave mode data set. This ends up with 1218 collocated data points. The spatial positions of these collocated wave buoys are shown in Fig. 9(a). Of which, 714 collocated data points are scattered along the east coast of the North America and 61 points off the west coast and the rest (443 points) are around the Hawaii. We first compared the significant wave height of buoys and WW3, which are in good consistency with negligible biases in Fig. 9(b). The averaged one-dimensional wave spectra from all the buoy measurements and the corresponding WW3 simulations are then given in Fig. 9(c). Both data sets present high conformity for most of the wavelengths, except at the long waves of 350 m where buoy tends to measure slightly larger wave spectral density. The two wave peaks are well captured by both WW3 and buoys. One is long swell (wavelength of 330 m) coming from remote storms in the Southern Ocean and the north extratropics. The other corresponds to locally generated wind sea at the wavelength of 120 m. This comparison well evidences the capability of WW3 in accurately modelling the one-dimensional ocean wave spectra.

However, the MACS profile derived from the SAR measurement, WW3-simulation and buoy-simulation show quite striking disagreement as shown in Fig. 9(d). At the low wavenumber (long wavelength), the averaged SAR MACS still displays the abrupt increase, while both WW3 and buoy are in good agreement with much lower spectral energy. Towards the higher wavenumber, the three data sets all show a decreasing trend but with different spectral level. In particular, the WW3-simulation predicts the highest MACS values, while buoy predicts the lowest. SAR-measured MACS profile lies in between and has comparable MACS with buoy-simulations for the waves shorter than 60 m. The differing MACS between the two simulation data set of WW3 and buoy contrasts their alignment in terms of the one-dimensional wave spectra in Fig. 9(a). This indicates that the directional pattern of both wave spectra might be different. To confirm, the mean wave direction as well as the spectral spread for both wind sea and swell part are calculated. The partition of wind sea from swell is based on the assumption of a fully developed sea state where the wind and waves are in equilibrium. The separation wavenumber k_s is set as the wavenumber where its phase speed equates the local wind speed. The mean wave direction and the directional spread are then computed in terms of the following formulas (Herbers et al., 1999)

$$tan\phi_m = \frac{\int_{k_0}^{k_1}\int_{-\pi}^{\pi} sin\phi S(k,\phi)dkd\phi}{\int_{k_0}^{k_1}\int_{-\pi}^{\pi} cos\phi S(k,\phi)dkd\phi} \quad (4)$$

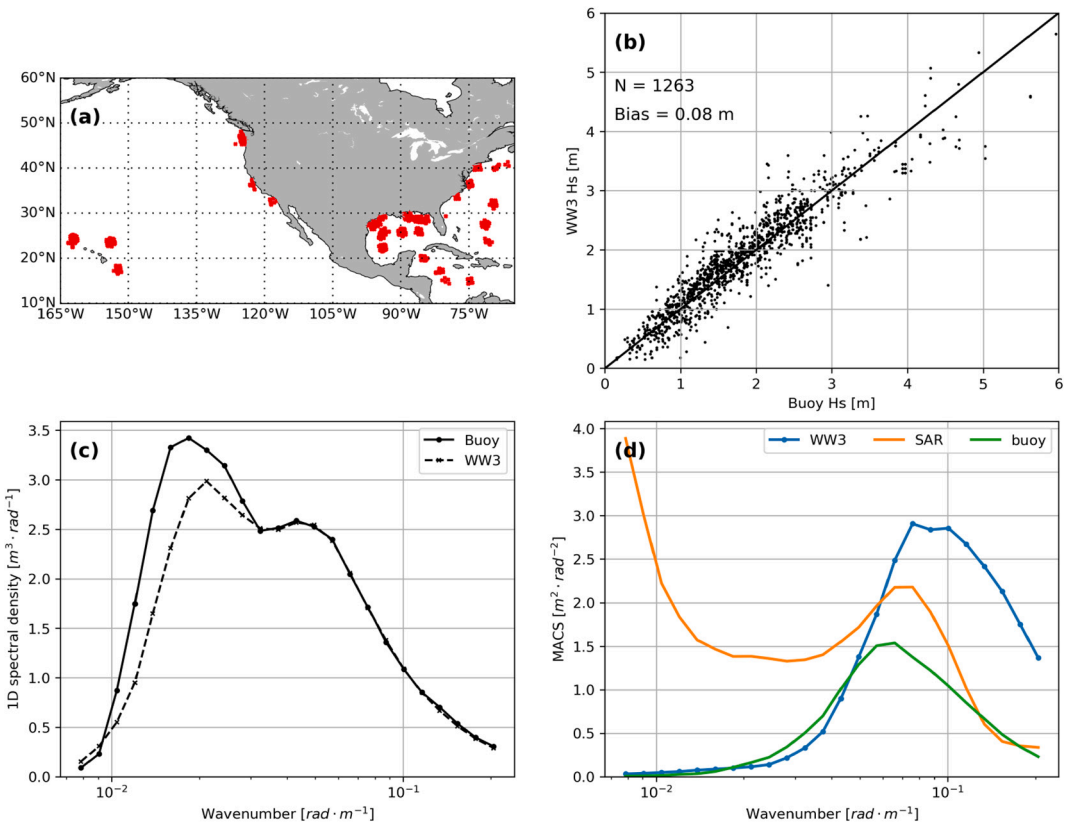

Fig. 9. Comparison of the triple collocation between SAR, buoy and WW3. (a) Position of NDBC buoys collocated with SAR observations in this study. (b) Comparison of the significant wave height between the collocated WW3 and buoys. (c) The one-dimensional wave spectrum is obtained by integrating over all wave directions and averaged for all the spectra from buoy and WW3, respectively. (d) The averaged MACS profile over all collocation pairs for the SAR-measured, WW3-simulated and buoy-simulated, respectively.

and

$$\sigma_{\phi}^{2} = \frac{\int_{k_0}^{k_1}\int_{-\pi}^{\pi} sin^2(\phi-\phi_m)S(k,\phi)dkd\phi}{\int_{k_0}^{k_1}\int_{-\pi}^{\pi} S(k,\phi)dkd\phi} \quad (5)$$

where k is the wavenumber and ϕ is the wave direction. For the wind sea, $k_0 = k_s$ and for the swell part, $k_1 = k_s$. $S(k,\phi)$ is the two-dimensional wave spectrum from the WW3 hindcast output or the buoy measurements.

The calculated mean wave direction and directional spread for both wind sea and swell part are presented in Fig. 10. As reflected by the metrics, the wave spectrum of both WW3 and buoy are consistent in terms of the swell partition. The mean swell direction of both data sets scatter tightly around the one-to-one line as shown in Fig. 10(a). While the swell direction spreads appears to loose relationship with large standard deviation in comparison to the magnitude. By comparison, bias of the mean wind sea direction in Fig. 10(c) is -8.97°, which is larger than that of the swell direction. Though bias of the spectral spread for wind sea is small of 1.16° (Fig. 10(d)), their correlation is 0.34 while the swell shows a correlation of 0.56 in Fig. 10(b). In addition, the linear slope of least-squared fit to these points is 0.24, which is also much smaller compared to the 0.71 for the swell in Fig. 10(b). The impact of wind sea on the simulated MACS profile is two-fold. On one hand, the slightly shifted wind sea direction might result in differing MACS magnitude along the range direction. On the other hand, the wind sea spread could cause the nonlinear velocity bunching to be vary between buoy and WW3 cases. This would accordingly change the magnitude of SAR image spectra as well as the MACS.

To demonstrate the impact of wave directional spread on the MACS profile, two SAR cross-spectra are simulated based on the JONSWAP spectrum and the following directional spreading function (Mitsuyasu et al., 1975):

$$D(k,\phi) = \left|cos\left[\left(\phi-\overline{\phi}\right)\Big/2\right]\right|^{(2s)} \quad (6)$$

where ϕ is the wave direction and $\overline{\phi}$ denotes the dominant wave direction. The parameter s determines the concentration degree of the spreading function relative to the mean direction. For simplicity, two constant values of $s = 2$ and $s = 8$ are set to calculate the directional wave spectra as shown in Fig. 11 (a). The contour lines represent the 25% and 75% of the maximum wave spectral energy, respectively. The mean wave direction is 45° from the azimuth, the wind speed is $8m \cdot s^{-1}$ and the wind fetch is 500 km. The wave spectrum of $s = 2$ (blue curve) displays wider spread compared to that of $s = 8$ (orange curve). The combined effect of wave direction deviation from the range axis and the wider spread function for $s = 2$ results in larger wave spectra magnitude along the radar line-of-sight. In consequence, the simulated image spectra of $s = 2$ shown in Fig. 11 (c) is larger than that of $s = 8$ in Fig. 11 (b) in the range direction. This corresponds to the higher MACS profile simulated based on the wide-spread wave spectrum (blue curve) as given in Figure (d). Note that the configuration of mean wave direction is similar to that of the mean wind sea direction in Fig. 10. The results that larger direction spread yields higher MACS profile, in accordance with the slightly greater wind sea direction spread in Fig. 10(d), to some extent explain the MACS comparison in Fig. 9(d). Further in-depth and comprehensive evaluation of the WW3 outputs relative to the buoy measurements in terms of the spectral perspective, rather than the significant wave height should be devised.

4. Discussion

As a parameter defined relative to the variable wavelengths, MACS

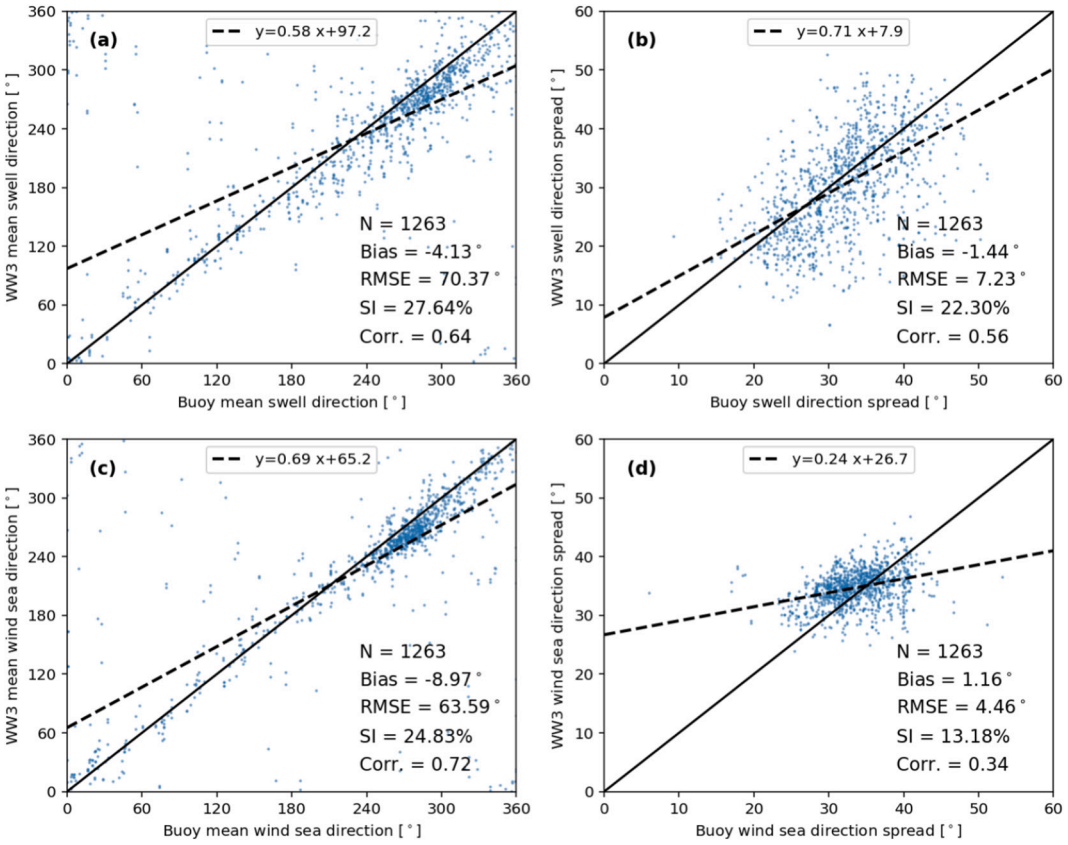

Fig. 10. Comparison of the mean swell in (a) and wind sea direction in (c) between the WW3 outputs and buoy observations with the directional spread accordingly shown in (b) and (d). Metrics are annotated on the bottom right of each plot.

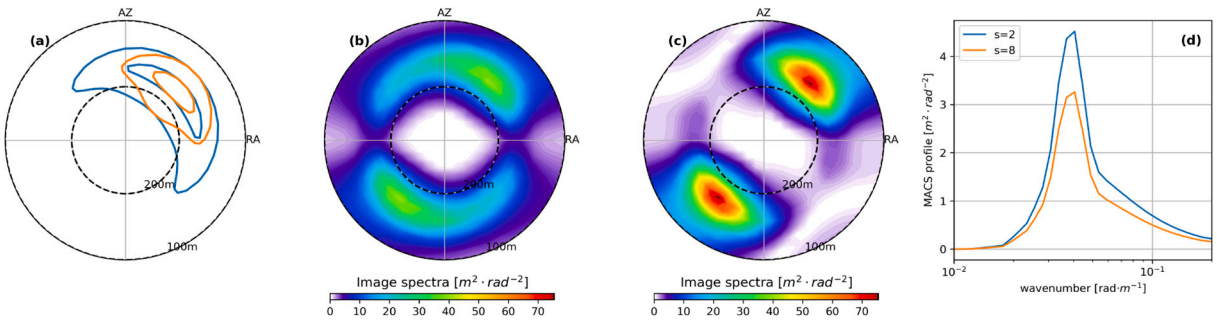

Fig. 11. (a) The normalized directional wave spectrum for $s = 2$ (blue curve) and $s = 8$ (orange curve) in Eq. (6). The contour lines give the 25% and 75% relative to the maximum spectral energy. The simulated SAR image cross-spectrum is given in (b) $s = 2$ and (c) $s = 8$, respectively. (d) The accordingly extracted MACS profile. (For interpretation of the references to color in this figure legend, the reader is referred to the web version of this article.)

offers new perspectives to devise comparisons between SAR observations and the reference data set. In this study, we find that the global patterns of SAR-observed MACS promisingly resemble that of the WW3-simulation. Yet the quantitative disagreements are noticeable. As demonstrated by the percentile analyses of MACS profile in Fig. 3, SAR and WW3 have particularly marked difference for the long waves (wavelength longer than 300 m) and wind sea (wavelength shorter than 100 m). The MACS overestimation of wind sea by the WW3-simulation is consistent across the open ocean as shown in Fig. 6(a). While the difference for long waves is region dependent (see Fig. 6(c)). As illustrated in Fig. 1, the image spectrum for long wavelengths derived from SAR observations are subject to impact of atmospheric and/or oceanic features on the sea surface, which pollutes the wave signals in the MACS analyses. In fact, the influence of large-scale features on the radar backscatter also depends on the local wind speed. As concluded in (Wang et al., 2019), the rain is difficult to be identified particularly at high winds. As such, its impact on the image cross-spectra for long wavelength is negligible so that $MACS_{342}$ has consistent values for both R1 and R3 regions in the extratropics. While the rain impact at low winds are expected to be significant, for example for R2 in the trade winds, SAR-observed $MACS_{342}$ is much higher as shown in Fig. 8(b3).

A test is performed as a first attempt to illustrate the impact of large-scale features on the MACS estimates. In general, SAR image spectra of these patterns have an unusually high tail at low wavenumber of MACS profile similar to that in Fig. 1(d4). A simplified criteria is employed to sort out the cases with such high-tail form. If the averaged MACS for wavelengths longer than 342 m is larger than its counterpart for shorter wavelengths (<342 m), this case is assumed to be impacted by the large-scale features. Otherwise, ocean wave signatures are expected to dominate in this case. The histogram of MACS for two wavelengths of 342 m and 453 m is presented in Fig. 12 calculated for these two classes, respectively. For SAR-measured MACS in Fig. 12(a), all cases with large-scale features tend to have larger MACS magnitude in comparison to the cases with dominant waves. The two curves of $MACS_{342}$ (blue) are closer to each other in comparison to those of $MACS_{453}$ (orange). This is indicative of the enlarging impact of these large-scale features with wavelengths. While WW3 wave spectra are only able to predict surface wave properties, the MACS contrast between the pure waves (solid line) and potential large-scale (dashed) in Fig. 12(b) is not as evident as that in Fig. 12(a). Given the non-negligible difference shown in Fig. 12(a), processing steps are essential to identify the presence of large-scale phenomena and filter out their contributions in the SAR image spectrum for a proper interpretation of the image cross-spectra. As a matter of fact, on-going efforts are being made to classify these features based on a deep learning technique for Sentinel-1 observations. Valid algorithms are expected to be deployed and a consistent reprocessing from ASAR to Sentinel-1 shall then be feasible for the improved wave retrieval.

5. Summary

Despite the previously extensive studies to evaluate the SAR wave observations based on the subrange wave height (Li and Saulter, 2012), the capability of SAR mapping isolated wave component remains undisclosed. This study further advances the SAR wave validation towards the image spectral level through the newly defined MACS parameter. One of its advantages is its versatility, allowing the comparison to be directly made for various wavelengths without the nonlinear SAR inversion scheme.

The large volume of data acquired by Envisat/ASAR aids the examination of MACS relationships with respect to the collocated WW3 hindcast wave spectra. Both data sets show a couple of similarities in terms of the MACS signatures. First of all, MACS magnitudes of all wavelengths are comparable between SAR-measured and WW3-simulation. The global patterns of SAR- and WW3-derived MACS agree well with high correlations in the open ocean. However, the quantitative inconsistency between these two is not only wavelength variant, but also regionally dependent. WW3 appears to constantly predict larger MACS

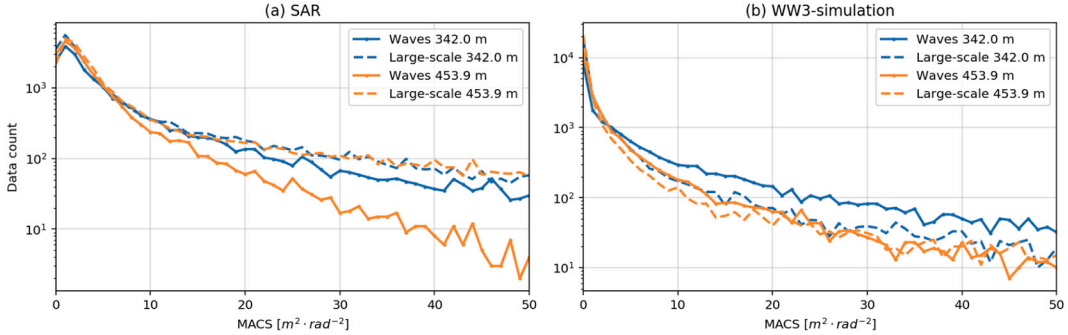

Fig. 12. Histogram of the (a) SAR-measured and (b)WW3-simulated $MACS_{342}$ and $MACS_{453}$ with (dashed curves) and without (solid curves) the potential impact of large-scale features on SAR images.

magnitude for the short wind sea (λ<100 m) at global scale. For the long waves (λ>300 m), such overestimate by the WW3-simulation only exhibits in the southern extratropics with opposite trend in the trade winds where WW3 predicts consistently smaller values. In contrast to the well aligned significant wave height (Li and Saulter, 2012; Stopa and Mouche, 2017), the difference observed by MACS of various wave scales is expected to offer new insights into the assessment approach of SAR observations.

Even with the assumption that the SAR forward transformation used in this paper is able to accurately reproduce the wave imaging process, several points still need to be addressed in order to better interpret the results of MACS comparison. On one hand, the large-scale impact should be further quantified as effort to isolate the MACS quantity that is associated with ocean surface waves. This will in turn help refine the SAR wave inversion and further enhance the utility of SAR measurements in accurately illustrating the ocean swell partitions. For example, taking the WW3 wave spectrum as the absolute reference data, the input real aperture radar (RAR) modulation transfer function (MTF) could be adjusted to match the SAR-measured values. This shall devise a more comprehensive RAR MTF relative to wave scales at various wind conditions as in (Romeiser et al., 1994), which can be readily used to the wave inversion. In addition, other geophysical applications, such as air-sea interactions and sea ice monitoring shall also benefit. On the other hand, the spectral spread has been demonstrated to have impact on the MACS magnitude along with the mean wave direction. The inconsistency observed between buoy-based and WW3-based simulations also invokes the necessity of validating the numerical outputs in terms of the two-dimensional wave spectra rather than the integrated parameters.

In this paper, we focused on the assessment of MACS profile from the Envisat/ASAR wave mode observations. There are also multiple SAR sensors in orbit now, including Sentinel-1 constellation, Radarsat Constellation Mission, Gaofen-3 et al. Instrument characteristics, such as spatial resolution, swath and incidence angles, generally differ among these satellites. While the commonly used validation procedure through significant wave height is limited to evaluate the SAR wave measurements. This MACS approach can be readily extended to grade the performance of SAR observations from the spectral point of view as well as to determine the consistency between sensors.

Credit author statement

Huimin Li carried out the data analysis and prepared the manuscript; Justin Stopa and Alexis.

Mouche analyzed the results and revised the manuscript; Biao Zhang, Yijun He and Bertrand.

Chapron discussed the results.

Declaration of Competing Interest

None.

Acknowledgments

This study is supported in part by the National Science Foundation of China (under grant 42006163, 42027805, 42076181 and 41620104003), in part by the Startup Foundation for Introducing Talent of NUIST, in part by the European Space Agency under grant of Sentinel-1 Mission Performance Center (Contract No. 4000107360/12/I-LG) and S1-4SCI Ocean Study project (Contract No. 4000115170/15/I-SBo), in part by the Centre National D'études Spatiales (TOSCA program, COWS project). The ECMWF reanalysis winds are obtained in the framework of Sentinel-1 Mission Performance Center and are publicly available (ecmwf.int). The wave buoy data are provided by NDBC and publicly available *via* https://www.ndbc.noaa.gov/.

References

Ardhuin, F., Rogers, E., Babanin, A.V., Filipot, J.F., Magne, R., Roland, A., van der Westhuysen, A., Queffeulou, P., Lefevre, J.M., Aouf, L., et al., 2010. Semiempirical dissipation source functions for ocean waves. Part i: definition, calibration, and validation. J. Phys. Oceanogr. 40, 1917–1941. https://doi.org/10.1175/2010jpo4324.1.

Ardhuin, F., Stopa, J., Chapron, B., Collard, F., Smith, M., Thomson, J., Doble, M., Blomquist, B., Persson, O., Collins, C.O., Wadhams, P., 2017. Measuring ocean waves in sea ice using sar imagery: a quasi-deterministic approach evaluated with sentinel-1 and in situ data. Remote Sens. Environ. 189, 211–222. URL. http://www.sciencedirect.com/science/article/pii/S0034425716304710. https://doi.org/10.1016/j.rse.2016.11.024.

Collard, F., Ardhuin, F., Chapron, B., 2009. Monitoring and analysis of ocean swell fields from space: New methods for routine observations. J. Geophys. Res. Oceans 114, 1–15. URL: https://agupubs.onlinelibrary.wiley.com/doi/abs/10.1029/2008JC005215, doi: 10.1029/2008JC005215, arXiv:https://agupubs.onlinelibrary.wiley.com/doi/pdf/10.1029/2008JC005215.

Engen, G., Johnsen, H., 1995. Sar-Ocean wave inversion using image cross spectra. IEEE Trans. Geosci. Remote Sens. 33, 1047–1056. https://doi.org/10.1109/36.406690.

Hasselmann, S., Hasselmann, K., 1985. Computations and parameterizations of the nonlinear energy transfer in a gravity-wave spectrum. Part i: a new method for efficient computations of the exact nonlinear transfer integral. J. Phys. Oceanogr. 15, 1369–1377. https://doi.org/10.1175/1520-0485(1985)015<1369:CAPOTN>2.0.CO;2.

Hasselmann, K., Barnett, T., Bouws, E., Carlson, H., Cartwright, D., Enke, K., Ewing, J., Gienapp, H., Hasselmann, D., Kruseman, P., Meerburg, A., Müller, P., Olbers, D., Richter, K., Sell, W., Walden, H., 1973. Measurements of wind-wave growth and swell decay during the Joint North Sea Wave Project (JONSWAP). In: Part of collection: Hydraulic Engineering Reports A, 8. Deutches Hydrographisches Institut, Hamburg, Germany, p. 12.

Hasselmann, K., Chapron, B., Aouf, L., Ardhuin, F., Collard, F., Engen, G., Hasselmann, S., Heimbach, P., Janssen, P., Johnsen, H., Krogstad, H., Lehner, S., Li, J.G., Li, X.M., Rosenthal, W., Schulz-Stellenfleth, J., 2012. The Ers Sar Wave Mode – A Breakthrough in Global Ocean Wave Observations. URL. https://elib.dlr.de/77565/.

Herbers, T.H.C., Elgar, S., Guza, R.T., 1999. Directional spreading of waves in the nearshore. J. Geophys. Res. Oceans 104, 7683–7693. URL: https://agupubs.onlinelibrary.wiley.com/doi/abs/10.1029/1998JC900092, doi: 10.1029/1998JC900092, arXiv:https://agupubs.onlinelibrary.wiley.com/doi/pdf/10.1029/1998JC900092.

Johnsen, H., 2005. ENVISAT ASAR Wave Mode Product Description and Reconstruction Procedure. Technical Report 1/2005. Norut. Tromso, Norway.

Kerbaol, V., Chapron, B., Vachon, P.W., 1998. Analysis of ERS-1/2 synthetic aperture radar wave mode imagettes. J. Geophys. Res. Oceans 103, 7833–7846. https://doi.org/10.1029/97jc01579.

Krogstad, H.E., Samset, O., Vachon, P.W., 1994. Generalizations of the non-linear ocean-sar transform and a simplified sar inversion algorithm. Atmosphere-Ocean 32, 61–82. https://doi.org/10.1080/07055900.1994.9649490.

Li, J.G., Saulter, A., 2012. Assessment of the updated Envisat ASAR Ocean surface wave spectra with buoy and altimeter data. Remote Sens. Environ. 126, 72–83. https://doi.org/10.1016/j.rse.2012.08.018.

Li, H., Chapron, B., Mouche, A., Stopa, J.E., 2019a. A new ocean sar cross-spectral parameter: Definition and directional property using the global sentinel-1 measurements. J. Geophys. Res. Oceans 124, 1566–1577. https://doi.org/10.1029/2018JC014638.

Li, H., Mouche, A., Wang, H., Stopa, J.E., Chapron, B., 2019b. Polarization dependence of azimuth cutoff from quad-pol sar images. IEEE Trans. Geosci. Remote Sens. 1–10. https://doi.org/10.1109/TGRS.2019.2929835.

Lygre, A., Krogstad, H.E., 1986. Maximum entropy estimation of the directional distribution in ocean wave spectra. J. Phys. Oceanogr. 16, 2052–2060. https://doi.org/10.1175/1520-0485(1986)016<2052:MEEOTD>2.0.CO;2.

Mitsuyasu, H., Tasai, F., Suhara, T., Mizuno, S., Ohkusu, M., Honda, T., Rikiishi, K., 1975. Observations of the directional spectrum of ocean wavesusing a cloverleaf buoy. J. Phys. Oceanogr. 5, 750–760. URL: doi: 10.1175/1520-0485(1975)005<0750:OOTDSO>2.0.CO;2, doi: 10.1175/1520-0485(1975)005<0750:OOTDSO>2.0.CO;2, arXiv:https://journals.ametsoc.org/jpo/article-pdf/5/4/750/4603070/1520-0485(1975)005_0750_ootdso_2_0_co_2.pdf.

Nagarajan, B., Aiyyer, A.R., 2004. Performance of the ecmwf operational analyses over the tropical indian ocean. Mon. Weather Rev. 132, 2275–2282. https://doi.org/10.1175/1520-0493(2004)132<2275:POTEOA>2.0.CO;2.

Pleskachevsky, A., Jacobsen, S., Tings, B., Schwarz, E., 2019. Estimation of sea state from sentinel-1 synthetic aperture radar imagery for maritime situation awareness. Int. J. Remote Sens. 40, 4104–4142. https://doi.org/10.1080/01431161.2018.1558377.

Quach, B., Glaser, Y., Stopa, J.E., Mouche, A.A., Sadowski, P., 2020. Deep learning for predicting significant wave height from synthetic aperture radar. IEEE Trans. Geosci. Remote Sens. 1–9. https://doi.org/10.1109/TGRS.2020.3003839.

Queffeulou, P., 2004. Long-term validation of wave height measurements from altimeters. Mar. Geod. 27, 495–510. https://doi.org/10.1080/01490410490883478.

Rikka, S., Pleskachevsky, A., Jacobsen, S., Alari, V., Uiboupin, R., 2018. Meteo-marine parameters from sentinel-1 Sar imagery: towards near real-time services for the Baltic Sea. Remote Sens. 10 https://doi.org/10.3390/rs10050757.

Romeiser, R., Schmidt, A., Alpers, W., 1994. A three-scale composite surface model for the ocean wave-radar modulation transfer function. J. Geophys. Res. Oceans 99, 9785–9801. https://doi.org/10.1029/93JC03372.

Saha, S., Moorthi, S., Pan, H.L., Wu, X., Wang, J., Nadiga, S., Tripp, P., Kistler, R., Woollen, J., Behringer, D., Liu, H., Stokes, D., Grumbine, R., Gayno, G., Wang, J., Hou, Y.T., Chuang, H.y., Juang, H.M.H., Sela, J., Iredell, M., Treadon, R., Kleist, D., Van Delst, P., Keyser, D., Derber, J., Ek, M., Meng, J., Wei, H., Yang, R., Lord, S., van den Dool, H., Kumar, A., Wang, W., Long, C., Chelliah, M., Xue, Y., Huang, B., Schemm, J.K., Ebisuzaki, W., Lin, R., Xie, P., Chen, M., Zhou, S., Higgins, W., Zou, C. Z., Liu, Q., Chen, Y., Han, Y., Cucurull, L., Reynolds, R.W., Rutledge, G., Goldberg, M., 2010. The ncep climate forecast system reanalysis. Bull. Am. Meteorol. Soc. 91, 1015–1058. https://doi.org/10.1175/2010BAMS3001.1.

Saha, S., Moorthi, S., Wu, X., Wang, J., Nadiga, S., Tripp, P., Behringer, D., Hou, Y.T., Chuang, H.Y., Iredell, M., Ek, M., Meng, J., Yang, R., Mendez, M.P., van den Dool, H., Zhang, Q., Wang, W., Chen, M., Becker, E., 2014. The ncep climate forecast system version 2. J. Clim. 27, 2185–2208. https://doi.org/10.1175/JCLI-D-12-00823.1.

Schulz-Stellenfleth, J., König, T., Lehner, S., 2007. An empirical approach for the retrieval of integral ocean wave parameters from synthetic aperture radar data. J. Geophys. Res. Oceans 112, 1–14. URL: https://agupubs.onlinelibrary.wiley.com/doi/abs/10.1029/2006JC003970, doi: 10.1029/2006JC003970, arXiv:https://agupubs.onlinelibrary.wiley.com/doi/pdf/10.1029/2006JC003970.

Stopa, J.E., 2018. Wind forcing calibration and wave hindcast comparison using multiple reanalysis and merged satellite wind datasets. Ocean Model 127, 55–69. https://doi.org/10.1016/j.ocemod.2018.04.008.

Stopa, J.E., Mouche, A., 2017. Significant wave heights from sentinel-1 sar: Validation and applications. J. Geophys. Res. Oceans 122, 1827–1848. URL: https://agupubs.onlinelibrary.wiley.com/doi/abs/10.1002/2016JC012364, doi: 10.1002/2016JC012364, arXiv:https://agupubs.onlinelibrary.wiley.com/doi/pdf/10.1002/2016JC012364.

Stopa, J.E., Ardhuin, F., Babanin, A., Zieger, S., 2016a. Comparison and validation of physical wave parameterizations in spectral wave models. Ocean Model. 103, 2–17. URL: http://www.sciencedirect.com/science/article/pii/S1463500315001614, doi: 10.1016/j.ocemod.2015.09.003. waves and coastal, regional and global processes.

Stopa, J.E., Ardhuin, F., Husson, R., Jiang, H., Chapron, B., Collard, F., 2016b. Swell dissipation from 10 years of envisat advanced synthetic aperture radar in wave mode. Geophys. Res. Lett. 43, 3423–3430. URL: https://agupubs.onlinelibrary.wiley.com/doi/abs/10.1002/2015GL067566, doi: 10.1002/2015GL067566, arXiv:https://agupubs.onlinelibrary.wiley.com/doi/pdf/10.1002/2015GL067566.

Stopa, J.E., Ardhuin, F., Stutzmann, E., Lecocq, T., 2019. Sea state trends and variability: consistency between models, altimeters, buoys, and seismic data (1979-2016). J. Geophys. Res. Oceans 3923–3940. https://doi.org/10.1029/2018jc014607.

Vandemark, D., Chapron, B., Elfouhaily, T., Campbell, J.W., 2005. Impact of high-frequency waves on the ocean altimeter range bias. J. Geophys. Res. Oceans 110. URL: https://agupubs.onlinelibrary.wiley.com/doi/abs/10.1029/2005JC002979, doi: 10.1029/2005JC002979, arXiv:https://agupubs.onlinelibrary.wiley.com/doi/pdf/10.1029/2005JC002979.

Wang, C., Tandeo, P., Mouche, A., Stopa, J.E., Gressani, V., Longepe, N., Vandemark, D., Foster, R.C., Chapron, B., 2019. Classification of the global sentinel-1 sar vignettes for ocean surface process studies. Remote Sens. Environ. 234, 111457. https://doi.org/10.1016/j.rse.2019.111457.

Young, I., 1999. Seasonal variability of the global ocean wind and wave climate. Int. J. Climatol. 19, 931–950. URL: https://rmets.onlinelibrary.wiley.com/doi/abs/10.1002/%28SICI%291097-0088%28199907%2919%3A9%3C931%3A%3AAID-JOC412%3E3.0.CO%3B2-O, doi: 10.1002/(SICI)1097-0088(199907)19:9<931::AID-JOC412>3.0.CO;2-O, arXiv:https://rmets.onlinelibrary.wiley.com/doi/pdf/10.1002/%28SICI%291097-0088%28199907%2919%3A9%3C931%3A%3AAID-JOC412%3E3.0.CO%3B2-O.

Young, I.R., Zieger, S., Babanin, A.V., 2011. Global trends in wind speed and wave height. Science 332, 451–455. URL: http://science.sciencemag.org/content/332/6028/451, doi: 10.1126/science.1197219, arXiv:http://science.sciencemag.org/content/332/6028/451.full.pdf.

Žagar, N., Skok, G., Tribbia, J., 2011. Climatology of the itcz derived from era interim reanalyses. J. Geophys. Res.-Atmos. 116, 1–6. URL: https://agupubs.onlinelibrary.wiley.com/doi/abs/10.1029/2011JD015695, doi: 10.1029/2011JD015695, arXiv:https://agupubs.onlinelibrary.wiley.com/doi/pdf/10.1029/2011JD015695.

Zieger, S., Vinoth, J., Young, I.R., 2009. Joint calibration of multiplatform altimeter measurements of wind speed and wave height over the past 20 years. J. Atmos. Ocean. Technol. 26, 2549–2564. https://doi.org/10.1175/2009JTECHA1303.1.